A composite with SiO$_x$ nanoparticles confined in carbon framework as an anode material for lithium ion battery†

Zixu Sun,[a] Xinghui Wang,[a] Tingwei Cai,[a] Zhen Meng[a] and Wei-Qiang Han*[ab]

A composite with ultrafine SiO$_x$ (x = 1.57, around 2 nm) nanoparticles confined in a carbon framework is synthesized by a simple thermopolymerization process and subsequent heat treatment. In the composite, the carbon framework can provide a consecutive network to improve the electrical conductivity of the composite and cushion the volume expansion to prevent the active material peeling from the current collector. The ultrafine SiO$_x$ nanoparticles can alleviate mechanical strain and shorten the diffusion/transport distance of lithium ions and electrons. In consequence, the as-synthesized composite delivers a high reversible capacity of 540 mA h g^{-1} at a current density of 500 mA g^{-1} after 200 cycles. The composite delivers good electrochemical performance, making it a promising candidate for the next-generation high-energy LIBs.

1. Introduction

Lithium-ion batteries (LIBs) with high energy density and long cycle life have extensive applications in portable electronic devices, transportation, and renewable energy storage.[1–8] Si-based materials are promising candidates to replace currently commercialized carbon materials due to their safety, abundance, and high theoretical specific capacity of 4200 mA h g^{-1}, which is much higher than that of graphite (372 mA h g^{-1}).[9–13] However, the application of Si-based materials is stopped by large volume expansion and low electrical conductivity,[14–17] resulting in pulverization of Si particles,[18] continuous solid electrolyte interface (SEI) film formation,[19] and rapid capacity loss.[20–22] Much attention has recently turned to SiO$_x$ ($0 < x \leq 2$) as an anode material for LIBs due to its low voltage and relatively stable cycling performance.[23–28] Compared to Si-based anodes, it undergoes much less volume expansion due to the inactive products of silicate/Li$_2$O, which can buffer the volume expansion.[24] Furthermore, amorphous state could deter the particle pulverization and fracture due to strain nonuniformity during charge/discharge process. However, the main barrier which limits the practical application of SiO$_x$-based materials is its low electrical conductivity, resulting in poor rate capability.[26,27]

To settle those issues, investigations on SiO$_x$-based materials with many strategies have been studied for solving the adverse effects and improving the electrochemical performance of SiO$_x$ anodes.[27–35] One strategy is to employ SiO$_x$ nanostructures of various morphologies, such as SiO$_2$ films,[36] hollow/porous structure,[28,34,35] which would be favorable for shortening the diffusion distance of Li$^+$ and enhancing rate capability of SiO$_x$. For example, hollow SiO$_2$ nanospheres were prepared for LIBs, and exhibited high cycle performance for 500 cycles.[34] Another strategy is to use SiO$_x$/carbon composites.[23,24,37,38] Carbon can not only enhance the electrical conductivity of the composite, but also suppress the aggregation of SiO$_x$ particles. Recently, Chen's group prepared nano-SiO$_2$/carbon composite as anodes for LIBs,[23] which presented a reversible capacity of 620 mA h g^{-1} at a current density of 100 mA g^{-1} after 300 cycles. Our previous report noted that hollow-silica–copper–carbon (H-SCC) nanocomposite showed a high reversible capacity as an anode for LIBs.[39] However, the electrochemical performance of SiO$_x$ is still not satisfactory and can't satisfy the demands for the practical application.

Here, we demonstrate a high reversible capacity and good cycling performance anode for LIBs. A composite, SiO$_x$ (x = 1.57) nanoparticles with a particle size of around 2 nm embedded in carbon framework (SiO$_x$/C NPs), is prepared by using tetraethoxysilane (TEOS) and phenol formaldehyde resin as silicon and carbon source, respectively. The carbon framework can prevent the SiO$_x$ nanoparticles from shedding, enhance the electrical conductivity of the composite, and accommodate the volume expansion of SiO$_x$ during charge–discharge process. The ultrafine SiO$_x$ nanoparticles can effectively decrease the diffusion/transport distance of lithium ions and electrons, alleviate the large strain of SiO$_x$ induced by Li$^+$ insertion/extraction. When used as an anode material for LIBs, the as-prepared SiO$_x$/C nanocomposite exhibits high capacity and excellent rate capability.

[a]Ningbo Institute of Materials Technology & Engineering, Chinese Academy of Sciences, Ningbo 315201, P. R. China

[b]Department of Materials Science and Engineering, Zhejiang University, Hangzhou 310027, P. R. China. E-mail: hanwq@zhu.edu.cn

2. Experimental

2.1 Materials preparation

In a typical preparation process, 1.0 g block copolymer F127 was dissolved in a mixture of 5.0 g of absolute ethyl alcohol and 1.0 g of 0.2 M HCl and stirred for 30 min at 40 °C to obtain a clear solution. Then, 1.58 g TEOS and 1.0 g phenol formaldehyde resin were added into the above solution, respectively. After stirred for 2 h at room temperature, the mixture was transferred into an oven at 100 °C for 24 h to thermopolymerize. The as-prepared products were ground into powders. The sample was thermally treated at 900 °C for 5 h under argon atmosphere with a ramping rate of 5 °C min^{-1} and then naturally cooled down to room temperature.

2.2 Characterization

XRD measurements were carried out using an AXS D8 Advance Diffractometer at a scanning rate of 2° min^{-1} in the range of 10–90°. The morphology of the samples was examined by a Hitachi S-4800 field emission scanning electron microscope (SEM) and an FEI Tecnai G2 F20 transmission-electron microscopy (TEM) with an accelerating voltage of 200 kV. The BET specific surface area was recorded by an ASAP 2020M (Micromeritics Instrument Corp., USA). FTIR measurements were conducted using a NICOLET 6700 machine (Thermo Fisher Scientific, USA). Thermal gravimetric analysis (TGA) was performed for the composite under air by a TGA machine (Pyris Diamond) employing at a heating rate of 10 °C min^{-1} to determine the content of SiO$_x$ in the composite. X-ray photoelectron spectroscopy (XPS, AXIS UTLTRA DLD, Japan) was measured for the composite.

2.3 Electrochemical tests

The electrodes were fabricated using the mixture the as-prepared composite, acetylene black and carboxymethyl cellulose (CMC) with a mass ratio of 8 : 1 : 1. Metallic lithium was used as the counter and reference electrode. The electrolyte was comprised of a 1 M LiPF$_6$ solution in fluoroethylene carbonate (FEC), dimethyl carbonate (DMC) and ethyl methyl carbonate (EMC) (1 : 1 : 1 by volume). Coin cells (CR 2032) were assembled in a glove box filled with high-purity argon. The charge–discharge tests were measured on a LAND CT2000 battery system within a voltage range of 0.01–1.5 V (vs. Li$^+$/Li). Cyclic voltammetry (CV) were performed on a CHI660 Electrochemical Workstation (Shanghai Chenhua) in a potential window from 0.01 to 1.5 V (vs. Li$^+$/Li) at a scan rate of 0.05 mV s^{-1}. Electrochemical impedance spectroscopy (EIS) were performed on a 1470E Electrochemical Interface (Solartron Analytical, UK) electrochemical workstation in the frequency ranging from 1 MHz to 10 mHz.

3. Results and discussion

Fig. 1 shows the fabrication procedure of a composite with confined SiO$_x$ nanoparticles in carbon framework. First, TEOS hydrolyzed and phenol formaldehyde resin thermopolymerized at 100 °C for 24 h. Then, the composite was synthesized by heat treatment at 900 °C for 5 h under argon atmosphere. XRD patterns of the SiO$_x$/C NPs are shown in Fig. 2a. The composite shows a broad peak at $2\theta = 22.1°$. Fig. 2b is the FTIR spectra of the SiO$_x$/C NPs. There are three peaks about at 1100, 801, and 472.6 cm^{-1} ascribed to SiO$_x$.[39] To obtain the weight of SiO$_x$ in
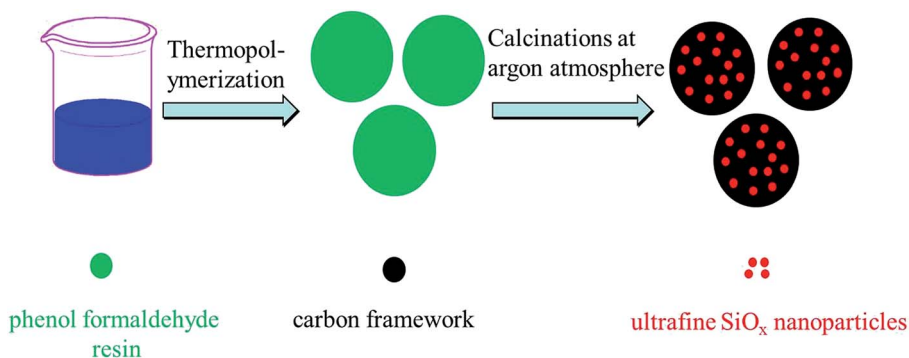

Fig. 1 Schematic illustration of the synthesis process of the SiO$_x$/C NPs.
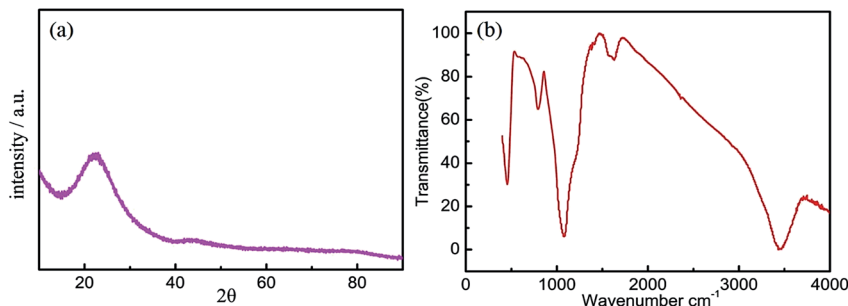

Fig. 2 (a) XRD patterns of the as-synthesized SiO$_x$/C NPs. (b) FTIR spectroscopy of the SiO$_x$/C NPs.
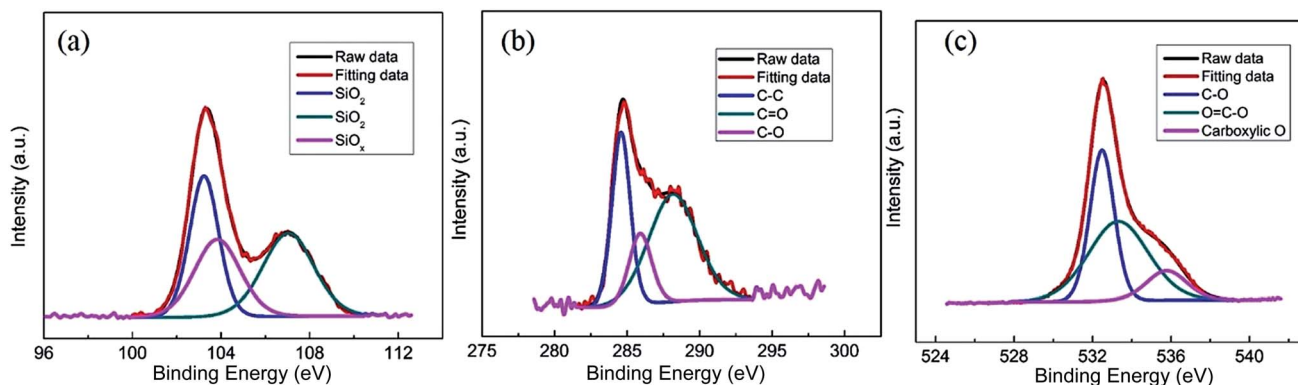
Fig. 3 XPS spectra for the SiO$_x$/C NPs: (a) Si 2p; (b) C 1s; (c) O 1s.

the composite, we carry out TGA experiment for the composite under air atmosphere. As shown in Fig. S1,† the SiO$_2$ content in the composite is about 83.71%. More detailed analysis is carried out using XPS measurements (Fig. 3). The results in Fig. 3a show

three peaks of the chemical bond types of silicon. The peaks at about 103.1 eV and 107.3 eV are SiO$_2$, and the peak at 104.0 eV corresponds to SiO$_x$.[40] The carbon in Fig. 3b is graphitic C at 284.4 eV. The other two types of C correspond to oxygen bridged
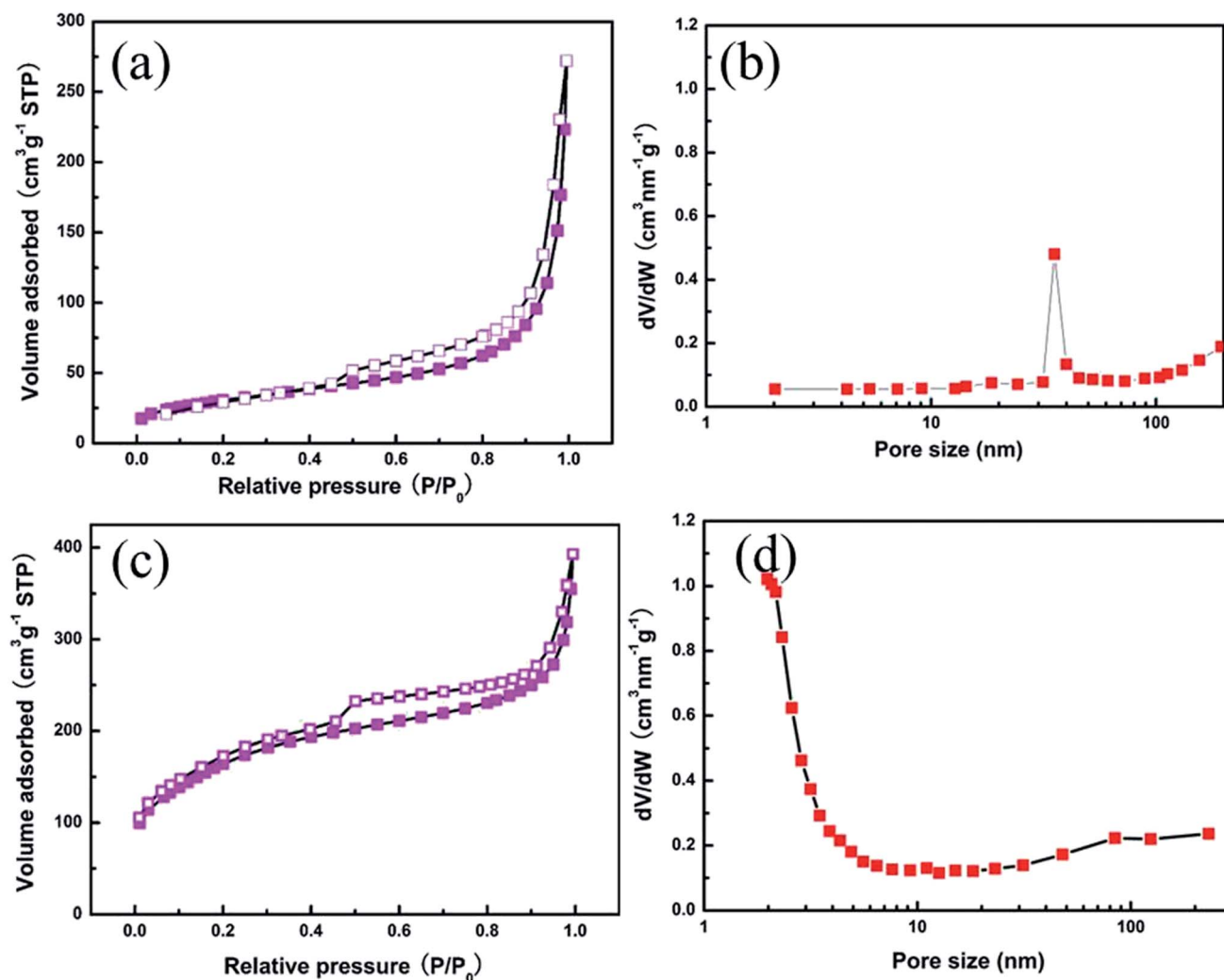

Fig. 4 adsorption–desorption isotherm (a) and pore size distribution (b) of the SiO$_x$/C NPs; adsorption–desorption isotherm (c) and pore size distribution (d) of the porous carbon.

C (C–O) at 286.6 eV, and aromatic C bonded with O (C═O) at 288.1 eV. As shown in Fig. 3c, three types of O bonding states are identified and corresponding to C–O 532.8 eV, O═C–O at 533.8 eV, and carboxylic O at 535.9 eV, respectively.

To gain the particle size distribution of SiO_x in the composite, the corrosion of the composite is conducted in 1.0 M NaOH aqueous solution for 4 h. After corrosion, the remaining substance is carbon and SiO_x dissolves. The N_2 absorption/desorption isotherms for the SiO_x/C NPs and porous carbon at 77 K are shown in Fig. 4. The specific surface area of the SiO_x/C NPs is around 111 $m^2 g^{-1}$ (Fig. 4a) and the pore size distribution of the SiO_x/C NPs possesses a mesoporous characteristic at around 37 nm (Fig. 4b), which may correspond to adsorption cumulative volume of the composite. After corrosion, Fig. 4c shows the characteristics of type IV with a hysteresis loop, demonstrating the existence of mesopores (2–50 nm) in porous carbon. The specific surface area of the porous carbon is about 596 $m^2 g^{-1}$. A narrow pore size distribution (2 nm) can be distinguished from Fig. 4d, compared with Fig. 4b. We can speculate that the composite can achieve high rate capabilities due to the following merits. First, high specific surface area can supply high contact area between electrolyte and SiO_x particles. Second, ultrafine SiO_x particles can shorten the diffusion/transport distance of lithium ions and electrons. Third, the carbon framework can enhance the electrical conductivity of the composite and restrain the volume expansion of SiO_x.

Fig. 5 displays the SEM images of the SiO_x/C NPs and porous carbon. The particle size distribution of the SiO_x/C NPs ranges from 20 to 50 nm, as shown in Fig. 5a and b. The as-prepared composite consists of the SiO_x nanoparticles and the carbon framework. The elemental composite of the SiO_x/C NPs is

determined by EDX, as shown in Fig. 5c and Table S1.† The contents of the Si, O, and C in the composite are 45.01%, 40.27% and 14.72%, respectively, which is in accordance with the TGA result. The atomic percentages of Si and O are 29.98% and 47.09%, respectively, corresponding to the atomic ratio of 1.57, which indicates that the value of x in the composite is 1.57. According to EDX results, the x value in SiO_x is about 1.57, and after TGA treatment, SiO_x is oxidized to SiO_2. According to the above analysis, we can estimate the SiO_x content in the composite is about 74.1%. The ultrafine SiO_x nanoparticles are embedded in carbon framework. After corrosion, there is no obvious change between the composite (Fig. 5a and b) and porous carbon (Fig. 5d and e), which indicates that NaOH aqueous solution doesn't damage the morphology of the composite. Fig. S2† shows the XRD patterns of porous carbon, which presents a weak and broad peak at around 24°. Fig. 5f and Table S2† show the elemental composite of the porous carbon, in which there are no other elements, indicating that SiO_x is completely corroded by the NaOH solution.

The energy dispersive X-ray spectra (EDS) mapping was used to characterize the element distribution of the composite. As shown in Fig. S3,† the Si, O, and C elements show a homogeneous distribution in the composite, which confirms that SiO_x nanoparticles are uniformly embedded into the carbon framework. More detailed morphologies and structure were determined by TEM. As shown in Fig. 6, TEM images of the SiO_x/C NPs show irregular morphologies, and the carbon framework is amorphous. TEM images indicate that the particle size of the SiO_x/C NPs is around 30 nm, which is consistent with the SEM results. From Fig. 6b, the ultrafine SiO_x particles with a size distribution of around 2 nm are embedded in the amorphous
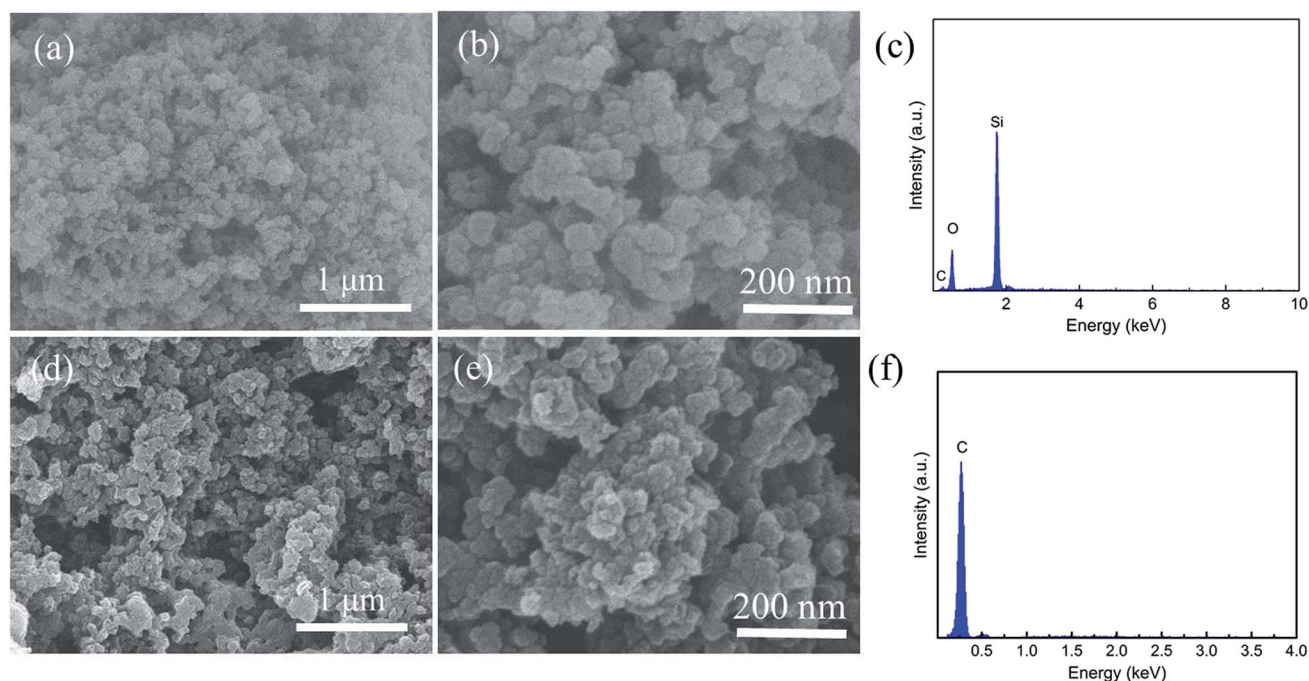

Fig. 5 Low- (a) and high- (b) magnified FESEM images of the SiO_x/C NPs, (c) EDX profile of SiO_x/C NPs. Low- (d) and high- (e) magnified FESEM images of products obtained after corrosion of the composite using 1.0 M NaOH aqueous solution, (f) EDX profile of porous carbon.
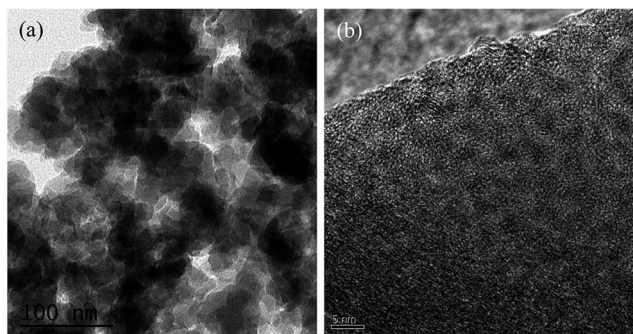
Fig. 6 (a) Low- and (b) high-magnified TEM images of the obtained SiO$_x$/C NPs.

carbon framework, which is in agreement with the BET results. Fig. S4† shows TEM image (a) and elemental mapping images (b) C, (c) O, (d) Si of the SiO$_x$/C NPs, which indicates that the three elements show a homogeneous distribution in the composite.

To evaluate the electrochemical performance of the SiO$_x$/C NPs, half cells using metallic lithium as the negative electrode are fabricated. The charge–discharge profiles of the composite are shown in Fig. 7a at a current density of 50 mA g^{-1} in a voltage window of 0.01–1.5 V. The first lithiation/delithiation capacities of the composite are 1457.9 and 646.6 mA h g^{-1}, respectively. The irreversible capacity loss during the first cycle may be ascribed to the formation of SEI layer and the reduction of the SiO$_x$ to Si.[40] The electrochemical reaction mechanism of SiO$_x$ are listed as follows, which has been reported before.[24]
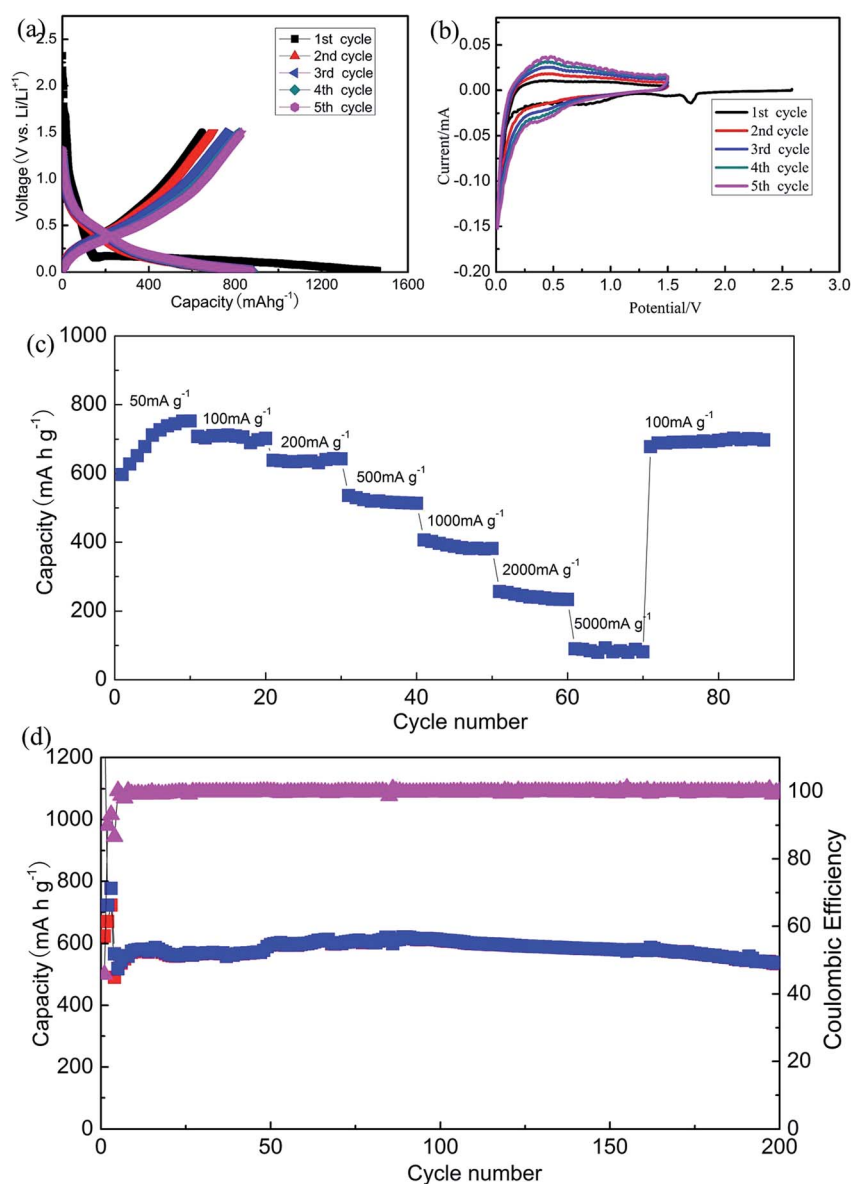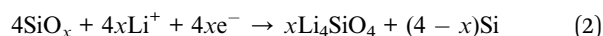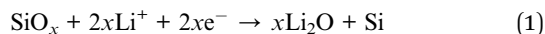

Fig. 7 (a) Galvanostatic charge/discharge profiles of the SiO$_x$/C NPs anode at a current density of 50 mA g^{-1}. (b) Cyclic voltammogram of the 1st to 5th cycle of the as-prepared SiO$_x$/C NPs between 0.01 and 1.5 V (*vs.* Li$^+$/Li) at a scanning rate of 0.05 mV s^{-1}. (c) Rate capability of the SiO$_x$/C NPs at different discharge currents. (d) Cycling performance of the SiO$_x$/C NPs electrode at a current density of 500 mA g^{-1}.

$$SiO_x + 2xLi^+ + 2xe^- \rightarrow xLi_2O + Si \qquad (1)$$

$$4SiO_x + 4xLi^+ + 4xe^- \rightarrow xLi_4SiO_4 + (4 - x)Si \qquad (2)$$

$$Si + xLi^+ + xe^- \leftrightarrow Li_xSi \qquad (3)$$

In the first discharge profile, there are a series of slopes between 0.6 and 1.7 V, which may be caused by the decomposition of electrolyte and the formation of SEI film. The slope at around 0.4 V is related to reaction (1) and reaction (2), which are corresponding to the formation of irreversible Li_2O and lithium silicate.[40] Then, the slope at around 0.1 V involves Si alloy reaction (reaction (3)), which is related to the lithiation of the first cycle and subsequent many cycles. The charge/discharge capacities of the composite gradually increase for subsequent cycles, which may be attributed to the activation of the anode material.[41] Fig. 7b shows CV curves of the composite in a potential window of 0.01–1.5 V (vs. Li^+/Li) at a scanning rate of 0.05 mV s^{-1} for the first 5 cycles. In the first half cycle, there are two reduction peaks at around 1.6 V and 0.85 V, respectively, which may be assigned to the decomposition of electrolyte and the formation of SEI film, which is in accordance with the above results. The following reduction peaks at around 0.4 and 0.1 V can be attributed to the irreversible formation of Li_2O and lithium silicate and Si alloying with Li. In the case of another half cycle, there is a broad peak at around 0.45 V, corresponding to the extraction of lithium ion from Li_xSi. From the CV curves, one can see that the peaks increase slightly with the cycles, demonstrating the activating process of SiO_x/C NPs during the initial cycles, which is in good agreement with the charge/discharge results.

Fig. 7c shows the rate capability of the SiO_x/C NPs. At a current density of 50 mA g^{-1}, the discharge capacity is stable at around 780 mA h g^{-1}. The capacities gradually decease with the increase of the current densities. Notably, it could still deliver a reversible capacity of ~90 mA h g^{-1} at a high current density of 5000 mA g^{-1}. Moreover, the capacity could recover to its original value when the current density goes back to 50 mA g^{-1}. The cycle performance of the composite at a current density of 500 mA h g^{-1} is shown in Fig. 7d. After activation for 3 cycles at a low current density of 50 mA g^{-1}, a stable capacity of around 540 mA h g^{-1} is obtained and no obvious capacity fading is observed even after 200 cycles, which is better than most previously reported results.[42,43]

To further find the reason for the excellent electrochemical performance of the SiO_x/C NPs electrode, EIS is performed with a applied amplitude of 5 mV. The frequency range is set from 1 MHz to 10 mHz, and EIS is performed on the composite after the 1st, 2nd and 50th cycle, respectively. The Nyquist plots consist of a depressed semicircle at high-frequency range and a straight line at low-frequency range. The diameter of the depressed semicircle corresponds to the resistance of the charge-transfer process of the electrode, while the straight line in the low frequency region represents the diffusion of Li ions in the SiO_x/C NPs electrode. From the Fig. 8, it can be seen that the charge-transfer resistance slightly increases even after 50
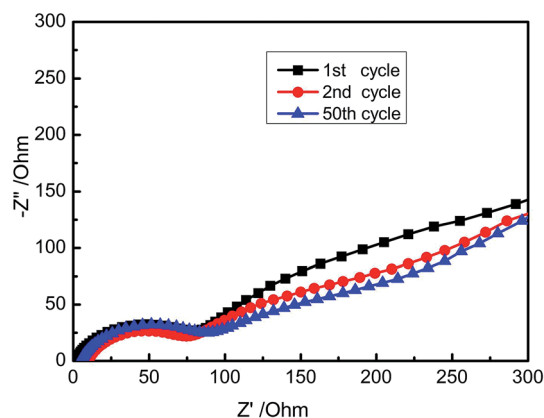

Fig. 8 Nyquist plots of the electrode of the SiO_x/C NPs after 1, 2 and 50 charge–discharge cycles at 50 mA g^{-1}, obtained after charging to 1.5 V.

charge–discharge cycles, demonstrating that the electrode has a stable interface and the good reaction kinetics during charge–discharge cycles, which is consistent with the good electrochemical performance of the SiO_x/C NPs electrode.

The good electrochemical performance could be attributed to the following facts: firstly, the carbon framework confined SiO_x nanoparticles can offer mechanical support to buffer the strain associated with the volume change, effectively enhance the electrical conductivity of the electrode, protect the SiO_x active material from the direct contact with electrolyte to avoid the continuous SEI film formation, and provide interconnected path for electrons and Li ions transport. Secondly, the ultrafine SiO_x nanoparticles (2 nm) can not only alleviate the stress induced by lithium ions insertion/extraction, but also decrease the diffusion/transport distance of lithium ions and electrons during charge/discharge process. Finally, the irreversible Li_2O and lithium silicate that formed during the first discharge process can buffer the strain induced by lithium ion insertion/extraction processes.

4. Conclusion

In summary, a novel composite for high-energy LIBs with a structure of the SiO_x nanoparticles confined in carbon framework is fabricated by a simple method. When evaluated as an anode material for LIBs, the as-synthesized composite exhibits good electrochemical performance. A high reversible capacity of around 540 mA h g^{-1} can be obtained at a current density of 500 mA g^{-1} after 200 cycles. This good electrochemical performance is ascribed to the carbon framework, which can supply conductive network to enhance the electrode electrical conductivity of the composite and buffer the volume expansion to prevent the aggregation, and the ultrafine SiO_x nanoparticles, which can shorten the diffusion/transport distance of lithium ions and electrons. The developed SiO_x/C NPs could be a promising anode material for the next-generation LIBs, and the fabrication method is simple, low-cost and scalable for mass production.

Acknowledgements

References

1 V. Etacheri, R. Marom, R. Elazari, G. Salitra and D. Aurbach, *Energy Environ. Sci.*, 2011, **4**, 3243.

2 Z. Yang, J. Zhang, M. C. W. Kintner-Meyer, X. Lu, D. Choi, J. P. Lemmon and J. Liu, *Chem. Rev.*, 2011, **111**, 3577–3613.

3 J. B. Goodenough and K.-S. Park, *J. Am. Chem. Soc.*, 2013, **135**, 1167–1176.

4 Z. Sun, C. Cao and W.-Q. Han, *RSC Adv.*, 2015, **5**, 72825–72829.

5 L. Zhou, H. Xu, H. Zhang, J. Yang, S. B. Hartono, K. Qian, J. Zou and C. Yu, *Chem. Commun.*, 2013, **49**, 8695–8697.

6 H. Zhang, X. Sun, X. Huang and L. Zhou, *Nanoscale*, 2015, **7**, 3270–3275.

7 H. Zhang, L. Zhou, O. Noonan, D. J. Martin, A. K. Whittaker and C. Yu, *Adv. Funct. Mater.*, 2014, **24**, 4337–4342.

8 H. Tian, F. Xin, X. Wang, W. He and W. Han, *Journal of Materiomics*, 2015, **1**, 153–169.

9 J. Zhao, Z. Lu, N. Liu, H. W. Lee, M. T. McDowell and Y. Cui, *Nat. Commun.*, 2014, **5**, 5088.

10 D. M. Piper, J. H. Woo, S. B. Son, S. C. Kim, K. H. Oh and S. H. Lee, *Adv. Mater.*, 2014, **26**, 3520–3525.

11 D. M. Piper, J. J. Travis, M. Young, S. B. Son, S. C. Kim, K. H. Oh, S. M. George, C. Ban and S. H. Lee, *Adv. Mater.*, 2014, **26**, 1596–1601.

12 S. Zhu, C. Zhu, J. Ma, Q. Meng, Z. Guo, Z. Yu, T. Lu, Y. Li, D. Zhang and W. M. Lau, *RSC Adv.*, 2013, **3**, 6141.

13 B. Wang, X. Li, B. Luo, Y. Jia and L. Zhi, *Nanoscale*, 2013, **5**, 1470–1474.

14 N. Lin, J. Zhou, Y. Zhu and Y. Qian, *J. Mater. Chem. A*, 2014, **2**, 19604–19608.

15 M. Gu, X.-C. Xiao, G. Liu, S. Thevuthasan, D. R. Baer, J.-G. Zhang, J. Liu, N. D. Browning and C.-M. Wang, *Sci. Rep.*, 2014, **4**, 7321–7327.

16 F. Sun, K. Huang, X. Qi, T. Gao, Y. Liu, X. Zou, X. Wei and J. Zhong, *Nanoscale*, 2013, **5**, 8586–8592.

17 O. Park, J.-I. Lee, M.-J. Chun, J.-T. Yeon, S. Yoo, S. Choi, N.-S. Choi and S. Park, *RSC Adv.*, 2013, **3**, 2538.

18 C. Chae, H.-J. Noh, J. K. Lee, B. Scrosati and Y.-K. Sun, *Adv. Funct. Mater.*, 2014, **24**, 3036–3042.

19 J. H. Byeon and Y.-W. Kim, *Adv. Mater. Interfaces*, 2014, **1**, 1300134.

20 N. Boaretto, A. Bittner, C. Brinkmann, B.-E. Olsowski, J. Schulz, M. Seyfried, K. Vezzù, M. Popall and V. Di Noto, *Chem. Mater.*, 2014, **26**, 6339–6350.

21 H. Liu, L. Hu, Y. S. Meng and Q. Li, *Nanoscale*, 2013, **5**, 10376–10383.

22 X. Li and L. Zhi, *Nanoscale*, 2013, **5**, 8864.

23 M. Li, Y. Yu, J. Li, B. Chen, X. Wu, Y. Tian and P. Chen, *J. Mater. Chem. A*, 2015, **3**, 1476–1482.

24 X. Yang, H. Huang, Z. Li, M. Zhong, G. Zhang and D. Wu, *Carbon*, 2014, **77**, 275–280.

25 Y. Yao, J. Zhang, L. Xue, T. Huang and A. Yu, *J. Power Sources*, 2011, **196**, 10240–10243.

26 J. M. Kim, Y. S. Huh, H. J. Kim, K. Song, S. H. Kim and H. S. Park, *Chem. Eng. J.*, 2014, **237**, 380–386.

27 B.-C. Yu, Y. Hwa, J.-H. Kim and H.-J. Sohn, *Electrochim. Acta*, 2014, **117**, 426–430.

28 J.-I. Lee and S. Park, *Nano Energy*, 2013, **2**, 146–152.

29 J.-J. Zhang, Z. Wei, T. Huang, Z.-L. Liu and A.-S. Yu, *J. Mater. Chem. A*, 2013, **1**, 7360–7369.

30 R. Zhou, W. Liu, X. Yao, Y. W. Leong and X. Lu, *J. Mater. Chem. A*, 2015, **3**, 16040–16049.

31 Y. Wang, W. Zhou, L. Zhang, G. Song and S. Cheng, *RSC Adv.*, 2015, **5**, 63012–63016.

32 M. Sasidharan, K. Nakashima, N. Gunawardhana, T. Yokoi, M. Ito, M. Inoue, S.-i. Yusa, M. Yoshio and T. Tatsumi, *Nanoscale*, 2011, **3**, 4768–4773.

33 L. Ji, Z. Lin, A. J. Medford and X. Zhang, *Carbon*, 2009, **47**, 3346–3354.

34 M. Sasidharan, D. Liu, N. Gunawardhana, M. Yoshio and K. Nakashima, *J. Mater. Chem.*, 2011, **21**, 13881–13888.

35 X. Feng, J. Yang, Q. Lu, J. Wang and Y. Nuli, *Phys. Chem. Chem. Phys.*, 2013, **15**, 14420–14426.

36 Q. Sun, B. Zhang and Z.-W. Fu, *Appl. Surf. Sci.*, 2008, **254**, 3774–3779.

37 J.-H. Kim, H.-J. Sohn, H. Kim, G. Jeong and W. Choi, *J. Power Sources*, 2007, **170**, 456–459.

38 Y. Kobayashi, S. Seki, Y. Mita, Y. Ohno, H. Miyashiro, P. Charest, A. Guerfi and K. Zaghib, *J. Power Sources*, 2008, **185**, 542–548.

39 Z. Sun, F. Xin, C. Cao, C. Zhao, C. Shen and W. Han, *Nanoscale*, 2015, 20426–20434.

40 W. Wu, J. Shi, Y. Liang, F. Liu, Y. Peng and H. Yang, *Phys. Chem. Chem. Phys.*, 2015, **17**, 13451–13456.

41 X. Wang, L. Sun, X. Hu, R. A. Susantyoko and Q. Zhang, *J. Power Sources*, 2015, **280**, 393–396.

42 J.-H. Kim, S. Lee and Y.-S. Lee, *J. Ind. Eng. Chem.*, 2015, **27**, 307–314.

43 Y. Ren, J. Ding, N. Yuan, S. Jia, M. Qu and Z. Yu, *J. Solid State Electrochem.*, 2012, **16**, 1453–1460.